Tomographic Sparse View Selection Using the View Covariance Loss

Jingsong Lin, *Graduate Student Member, IEEE*, Amirkoushyar Ziabari, *Senior Member, IEEE*, Singanallur V. Venkatakrishnan, *Senior Member, IEEE*, Obaidullah Rahman, Gregery T. Buzzard, *Senior Member, IEEE*, and Charles A. Bouman, *Life Fellow, IEEE*

(Invited Paper)

***Abstract*—Standard computed tomography (CT) reconstruction algorithms such as filtered back projection (FBP) and Feldkamp-Davis-Kress (FDK) require many views for producing high-quality reconstructions, which can slow image acquisition and increase cost in non-destructive evaluation (NDE) applications. Over the past 20 years, a variety of methods have been developed for computing high-quality CT reconstructions from sparse views. However, the problem of how to select the best views for CT reconstruction remains open. In this paper, we present a novel view covariance loss (VCL) function that measures the joint information of a set of views by approximating the normalized mean squared error (NMSE) of the reconstruction. We present fast algorithms for computing the VCL along with an algorithm for selecting a subset of views that approximately minimizes its value. Our experiments on simulated and measured data indicate that for a fixed number of views our proposed view covariance loss selection (VCLS) algorithm results in reconstructions with lower NRMSE, fewer artifacts, and greater accuracy than current alternative approaches.**

***Index Terms*—MBIR, sparse-view CT, tomography, view selection.**

I. Introduction

COMPUTED tomography (CT) is a widely used imaging tool in industrial non-destructive characterization. It enables visualization of the internal structure of scanned objects, aiding in the understanding of internal features, metrology and the detection of defects and anomalies [1]. A typical CT scan collects projections from different orientations around the object, also referred to as *views*, and a reconstruction algorithm then processes these projections to reconstruct an image or volume. Tuy's condition [2], [3] provides a general theory to determine the set of views required for perfect reconstruction. However, in practice, views are typically taken while the object is rotated around a single fixed axis.

Standard reconstruction methods are based on analytical techniques, such as filtered back projection (FBP) [4] for parallel-beam CT and the Feldkamp-Davis-Kress (FDK) algorithm [5] for cone-beam CT. Typically, the large array size of detectors requires the collection of many views so that analytical algorithms can generate high-quality reconstructions. For example, a detector with dimensions of 2000×2000 pixels generally needs about 2000 projection measurements at sufficiently high signal-to-noise ratio to achieve a high-quality $2000 \times 2000 \times 2000$ FDK reconstruction [6].

In non-destructive evaluation (NDE) for additive manufacturing (AM), the total scan time can vary from a few hours to a full day, depending on the system's energy and settings, the sample's density and size, and the desired resolution. However, these long scan times can limit the use of CT in NDE [7]. Consequently, AM inspection could greatly benefit from more effective methods of sparse-view acquisition and reconstruction.

To shorten scan times while preserving image quality, researchers have adopted sparse-view reconstruction methods. Techniques such as model-based iterative reconstruction (MBIR) [8], [9], [10], [11], plug-and-play (PnP) algorithms [12], [13], [14], and end-to-end deep learning (DL) methods [15], [16] have shown that high-quality reconstructions can be achieved with far fewer projections compared to the standard methods.

Using sparse-view reconstruction algorithms raises an important question: Given the limited number of projections available, which orientations should be selected to achieve the best reconstruction? Current workflows typically rely on measurements from a fixed, uniformly sampled set of orientations, without adapting to the unique geometry of the scanned object. However, empirical studies [17], [18] have shown that object-dependent scanning strategies can outperform uniform sampling in terms of reconstruction quality. For example, the Bruker High Aspect Ratio Tomography (HART) system [17] demonstrates that projections aligned with long, straight edges yield improved resolution in the reconstructed image. However, it is also crucial that

Received 15 July 2025; accepted 9 August 2025. Date of publication 19 August 2025; date of current version 4 September 2026. This work was supported in part by the DOE Office of Energy Efficiency and Renewable Energy (EERE) and in part by Advanced Materials and Manufacturing Technologies Office (AMMTO). The work of Charles A. Bouman was supported in part by the Showalter Trust. Recommended for acceptance by G. Wetzstein. *(Corresponding author: Charles A. Bouman.)*

Jingsong Lin is with the School of Electrical and Computer Engineering, Purdue University, West Lafayette, IN 47907 USA.

Amirkoushyar Ziabari, Singanallur V. Venkatakrishnan, and Obaidullah Rahman are with the Oak Ridge National Laboratory, Oak Ridge, TN 37830 USA.

Gregery T. Buzzard is with the Department of Mathematics, Purdue University, West Lafayette, IN 47907 USA.

Charles A. Bouman is with the School of Electrical and Computer Engineering, Purdue University, West Lafayette, IN 47907 USA (e-mail: bouman@purdue.edu).

This article has supplementary downloadable material available at https://doi.org/10.1109/TPAMI.2025.3600072, provided by the authors.

Digital Object Identifier 10.1109/TPAMI.2025.3600072

0162-8828 © 2025 IEEE. All rights reserved, including rights for text and data mining, and training of artificial intelligence and similar technologies. Personal use is permitted, but republication/redistribution requires IEEE permission. See https://www.ieee.org/publications/rights/index.html for more information.

Authorized licensed use limited to: Purdue University. Downloaded on September 14,2026 at 09:10:02 UTC from IEEE Xplore. Restrictions apply.

the selected projections remain diverse, rather than all clustering about a few prominent edge features.

While progress has been made in view selection (see Section II), determining the optimal views for CT reconstruction remains an open challenge. In particular, previous research tends to focus on criteria that favor views that are *individually most informative*, rather than criteria that favor view sets that are *jointly most informative.* This tends to result in view selection algorithms that do not incorporate the need for view diversity, or alternatively, incorporate diversity through ad-hoc heuristics requiring the manual selection of parameters.

In this paper, we introduce the view covariance loss selection (VCLS) algorithm to jointly select an optimal set of views based on a novel mathematical expression for what we call the view covariance loss (VCL). The VCL is a measure of the joint information contained in the set of views. It incorporates into a single loss function both a measure of the information contained in the individual views, as well as a measure of diversity among views. We derive the VCL from an expression for the normalized mean squared error (NMSE) when the volume is reconstructed using view-basis functions.

The key contributions of this paper are:

- Derivation of a novel closed-form parameter-free expression for the VCL loss function that measures the joint information contained in a set of views.
- Development of a VCLS algorithm that performs fast joint selection of view angles by approximately minimizing the VCL.
- Demonstration of the use and value of VCLS on large practical data volumes that are representative of NDE inspection applications for AM.

We apply the VCLS algorithm to the problem of cone-beam CT with a single fixed axis of rotation. Our approach assumes the availability of a "reference object" that can be used for the selection of views. For example, in AM, many manufactured versions of the same object design must typically be inspected for defects. In this case, the reference object can come from a scan of one of the many objects being inspected. However, if every object being manufactured is unique, then the reference object can come from a CAD model, which is typically available, or a quick pre-scan of the object being inspected. In each case, the VCLS algorithm uses the reference object to select the best view angles to scan during the inspection of the manufactured object(s).

Once the views are collected, we assume the volume is reconstructed using a sparse-view reconstruction algorithm, such as MBIR [19], since it provides higher-quality reconstructions from sparse-view data compared to standard techniques such as FDK.

Experimental results on simulated and measured cone-beam CT data show that the VCLS consistently outperforms both uniform view angle sampling as well as recent *ad hoc* strategies that combine view information with view diversity [20]. Also, leveraging MBIR reconstructions along with our proposed view angle selection results in fewer artifacts and offers sharper and more accurate edges.

An open source implementation of VCLS is available from [19] with examples and test data available at [21].

II. Related Work

Over the past 15 years, a variety of approaches have been proposed for object-dependent tomographic view selection. These approaches seek to select a fixed number of views in a manner that reduces artifacts, improves resolution, and/or reduces noise.

These approaches typically select view angles or other orientation parameters that attempt to maximize the useful information collected with each view. However, if one uses a completely greedy strategy of view selection, the result will be that too many similar views will be collected. Consequently, it is essential that views be collected so that they jointly maximize the information. This inevitably leads to a competing need for diversity in view selection.

For example, Batenburg et al. [22] considered the problem of view selection for the special case of binary tomography, in which the reconstruction is assumed to take on only two possible densities. In this case, they assumed that the total information of the projections was inversely proportional to the size of the set of binary solutions. However, this method does not naturally generalize to the tomographic reconstruction of continuously valued objects.

Several early approaches to view selection are based on the idea that views with higher-frequency content carry more information. For example, in Haque et al. [23], regions of projections with greater spectral richness are allocated a larger number of views. This non-uniform selection ensures that areas rich in information are sampled more densely. Similarly, in Presenti et al. [24], the objective is to select views that exhibit the largest intensity differences in the simulated projections generated from a CAD model.

Another related heuristic is that views aligned with the object's edges tend to contain more information, as they capture higher-frequency details and can enhance edge reconstruction quality. For example, in Matz et al. [25], views were selected that aligned with object edges detected using a wavelet transform analysis. In addition, another metric was employed to measure the angular distance between projections, thereby ensuring diversity in view selection.

In additive manufacturing applications, the edge information of the scanned objects can be directly extracted from the CAD model. In Yang et al. [26] and Lin et al. [20], [27], algorithms are proposed that construct an edge alignment function to evaluate how well each view aligns with the long edges present in the CAD model, as well as an angle dispersion function to assess the diversity of the views. By linearly combining these two functions with a weighting parameter λ, the methods can select views that align with long edges while ensuring sufficient diversity among the chosen views.

Other studies have utilized insights from CT design to improve scanning strategies. These insights include minimizing the path length through the object to reduce metal artifacts and photon starvation, as well as decreasing the variance of pixel values in a single projection to mitigate beam hardening artifacts. For example, in Heinzl et al. [28], the authors aim to determine the optimal placement of an object by minimizing the average or maximum path length through the material. Similarly, in Kano et al. [29], a comparable heuristic is applied, but with enhanced flexibility

Authorized licensed use limited to: Purdue University. Downloaded on September 14,2026 at 09:10:02 UTC from IEEE Xplore. Restrictions apply.

in controlling cone-beam parameters such as cone angle and tilt angle. In Ito et al. [30], two metrics are introduced—one for evaluating the path length through the object and another for assessing the variance in a single projection—to help identify an optimal rotation orientation for scanned objects. However, these approaches overlook the fact that certain orientations may have a long path length through the material yet still contain valuable information, such as long-edge information.

Task-based scanning strategy optimization is also an important research direction. For example, in [31], [32], [33], [34], methods are proposed to enhance defect detectability within a defined region of interest (ROI). In [34], this is achieved by optimizing the detectability index within the ROI, which quantifies how well a signal can be distinguished from noise in the frequency domain. The detectability index is determined by the modulation transfer function and the noise power spectrum of the reconstruction. These approaches leverage prior knowledge of the ROI to optimize the scanning trajectory, thereby reducing noise and improving image quality in critical areas. However, these methods are based on prior knowledge of the locations and geometries of defects.

Recent research has explored the use of deep learning for optimal view selection. For example, in [35], [36], [37], deep reinforcement learning (DRL) is employed to sequentially choose the next optimal view, using either projections or reconstructed images as input. These approaches frame the selection of optimal projections as a trajectory-based optimization problem and solve it using deep reinforcement learning. The reward function (i.e., the objective optimized during training) is primarily based on reconstruction loss. However, because of their computational complexity, these approaches have only been demonstrated for low-dimensional images.

In summary, previous research has developed object-dependent scanning strategies that outperform traditional object-independent approaches. However, aside from DRL-based methods, which do not easily scale to high-dimensional problems, the heuristic-based optimization frameworks used in these studies do not guarantee the selection of an optimal view set that directly minimizes reconstruction loss. These limitations motivate us to propose a new, computationally efficient loss function that directly guides the selection of views to minimize the reconstruction loss.

III. The View Covariance Loss (VCL)

We first derive an expression for a loss function that can be used to determine the best view subset of a reference object denoted by x. We assume here that our reference and test objects are similar so that the views selected for the reference object will result in a high-quality scan of the test object.

Depending on the details of the concept of operation, the reference object can be obtained from a scan of object that is similar to the test object, a CAD model of the test object, or a quick low-resolution pre-scan of the test object. We conclude the section by discussing the interpretation of the loss function and explaining how it can be efficiently computed for CT problems of practical size.

A. VCL Derivation

Let $\Omega = \{\theta_0, \ldots, \theta_{K-1}\}$ denote a set of scan view parameters that parameterize K tomographic views of an object. These parameters are typically scan angles in axial tomography, but they can represent anything that parametrizes each view of a scan.

For each view, we will assume that there is a corresponding reconstruction basis function, $T_{\theta_k} \in \mathbb{R}^N$, and that the object, x, can be approximately reconstructed as a linear combination of this set of view-basis functions. Mathematically, we can express this as

$$\hat{x}_{\Omega,\beta} = \sum_{k=0}^{K-1} T_{\theta_k}\beta_k = T_\Omega \beta \tag{1}$$

where

$$T_\Omega = [T_{\theta_0}, \ldots, T_{\theta_{K-1}}]$$

is an $N \times K$ matrix of view-basis functions and $\beta \in \mathbb{R}^K$ is a column vector of weights. Here, N is the number of voxels in the reconstruction and K is the number of views used to perform the reconstruction.

The selection of view-basis functions depends on the application. For example, in our CT reconstruction problem, if an analytical reconstruction algorithm such as FBP or FDK is used, then the reconstructed image is computed as a linear combination of filtered back-projections [38]. In this case, each view-basis function is chosen to be the filtered back projection (FBP) from a single view at angle θ_k

$$T_{\theta_k} = \alpha_{\theta_k}\text{FBP}(A_{\theta_k}x) = \alpha_{\theta_k}A_{\theta_k}^t H A_{\theta_k}x \tag{2}$$

where $A_{\theta_k}x$ represents the simulated forward projection of the reference object, x, at angle θ_k, H represents the required ramp filter that also depends on the choice of geometry [4], [5], and α_{θ_k} is any fixed scaling constant.

Based on this setup, our goal is to obtain the optimal reconstruction by minimizing the normalized mean squared error (NMSE) loss between x and $\hat{x}$ through the selection of the optimal subset given by

$$\Omega^* = \arg\min_{\Omega}\left\{\min_{\beta}\frac{\|x-\hat{x}_{\Omega,\beta}\|^2}{\|x\|^2}\right\} \tag{3}$$

where the reconstruction, $\hat{x}_{\Omega,\beta}$, depends on the selection of the set of view angles, Ω, and weights, β.

From this, we can see that our goal is to find the set of view angles, Ω^*, that minimizes the reconstruction distortion as shown below

$$\Omega^* = \arg\min_{\Omega} D(\Omega) \tag{4}$$

where $D(\Omega)$ is the NMSE in the reconstruction given by

$$D(\Omega) = \min_{\beta}\frac{\|x-\hat{x}_{\Omega,\beta}\|^2}{\|x\|^2}. \tag{5}$$

We can simplify the form of $D(\Omega)$ by calculating the optimal vector β_Ω^* for a specific choice of Ω. This is given by the solution

Authorized licensed use limited to: Purdue University. Downloaded on September 14,2026 at 09:10:02 UTC from IEEE Xplore. Restrictions apply.

to the following least-squares estimation problem.

$$\beta_\Omega^* = (T_\Omega^t T_\Omega)^{-1} T_\Omega^t x$$

Substituting β_Ω^* into (1) and (5) then results in

$$D(\Omega) = \frac{\|x - P_\Omega x\|^2}{\|x\|^2}$$

where $P_\Omega = T_\Omega (T_\Omega^t T_\Omega)^{-1} T_\Omega^t$. Note that P_Ω performs an orthogonal projection onto the column space of T. Consequently, the residual $x - P_\Omega x$ is orthogonal to the column space of T. Therefore, the norm squared $\|x - P_\Omega x\|^2$ can be computed using Pythagorean theorem

$$\|x - P_\Omega x\|^2 = \|x\|^2 - \|P_\Omega x\|^2 \tag{6}$$

where $\|P_\Omega x\|^2$ can be simplified as

$$\begin{aligned}\|P_\Omega x\|^2 &= x^t P_\Omega^t P_\Omega x \\ &= x^t T_\Omega \left(T_\Omega^t T_\Omega\right)^{-1} T_\Omega^t x \end{aligned} \tag{7}$$

and we use the fact that $P_\Omega^t P_\Omega = P_\Omega$ because P_Ω is an idempotent matrix. We can next use (6) and (7) to derive the following simplified expression for the NMSE.

$$\begin{aligned} D(\Omega) &= \frac{\|x - P_\Omega x\|^2}{\|x\|^2} \\ &= \frac{\|x\|^2 - \|P_\Omega x\|^2}{\|x\|^2} \\ &= 1 - \frac{x^t T_\Omega (T_\Omega^t T_\Omega)^{-1} T_\Omega^t x}{\|x\|^2} \end{aligned}$$

From this result, we can now write the NMSE reconstruction error as

$$D(\Omega) = L(R_\Omega, \gamma_\Omega) \tag{8}$$

where L is the view covariance loss (VCL) function defined by

$$L(R, \gamma) = 1 - \gamma^t R^{-1} \gamma. \tag{9}$$

and its arguments are given by

$$R_\Omega = T_\Omega^t T_\Omega \tag{10}$$

$$\gamma_\Omega = \frac{T_\Omega^t x}{\|x\|} \tag{11}$$

where R_Ω is the autocorrelation between the reconstruction bases, and γ is the correlation between the view bases and the reference object.

B. VCL Computation

Fig. 1 illustrates how the VCL is computed for a simple example of 8-view parallel-beam tomography. First, the filtered back-projection is computed for each view of the object. Then the matrix R is formed by the autocorrelation of the back-projected views, and the vector γ is formed by the cross-correlation between the views and the object. In the figure, we assume that $\alpha_\theta = 1/\|T_\theta\|$ in (2) so that the reconstruction bases are normalized. Consequently, the entries of both R and

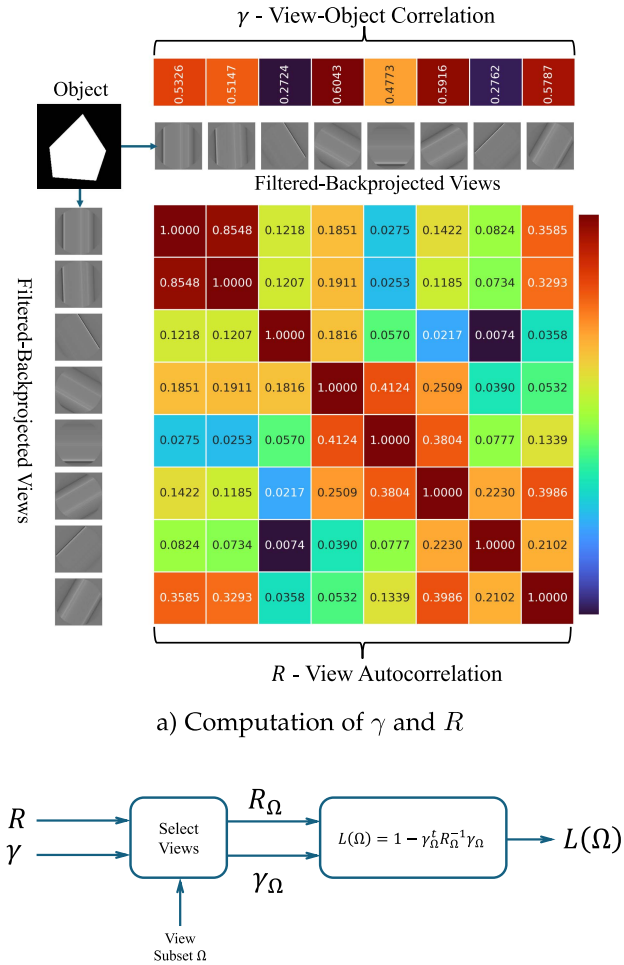


Fig. 1. Evaluation of the view covariance loss (VCL) for a toy example of parallel beam tomography with 8 views collected over 180°. (a) A typical object to be imaged is forward-projected, filtered, and back-projected to form views in the space domain. Then γ - the cross-correlation between the object and views is computed, and R - the autocorrelation between the views is computed. (b) The (R, γ) for the full set of views are subsampled to the selected views, and the resulting $(R_\Omega, \gamma_\Omega)$ are used to evaluate the loss function.

γ are normalized correlations so they take values in the range $[-1, 1]$, and R has 1's on its diagonal.

Here, $R \in \mathbb{R}^{K_{\max} \times K_{\max}}$ and $\gamma \in \mathbb{R}^{K_{\max}}$ where $K_{\max}$ corresponds to the largest set of views to be considered. Even for large practical problems, typically $K_{\max} \leq 2000$. Consequently, (R, γ) can be easily stored and used in calculations.

However, naive calculation of (R, γ) from the back-projected views can be very computationally expensive. This is because for large practical problems, each back projection can be very large; so computing and storing these back projections may not be practical. For example, for a reference object with an array size of $1024 \times 1024 \times 1024$ and 1000 candidate views, computing R requires evaluating approximately 5×10^5 inner products between two matrices, each with dimensions $1024 \times 1024 \times 1024$.

Fortunately, the computation and memory requirements for computing (R, γ) can be dramatically reduced by subsampling

Authorized licensed use limited to: Purdue University. Downloaded on September 14,2026 at 09:10:02 UTC from IEEE Xplore. Restrictions apply.



Fig. 2. (a) The CAD drawing used in the simulated data experiment; (b) axial slice of ground truth; and (c) axial slice of reference object used in view selection. Note that reference object is not identical to ground truth.

the reconstruction bases. Computing a single entry of R requires taking the inner-product of two very large reconstruction bases. However, sufficient accuracy can be achieved by computing the inner product using only a small randomly selected subset of voxels. Let $S \in \mathbb{R}^{N_S \times N}$ be a random sub-sampling matrix where $N_S << N$ is the number of sample voxels. In our experiments, we will choose $N_S = \lfloor r_1 N \rfloor$ where r_1 is a sampling rate parameter typically chosen to be very small. So then to compute the VCL using (9) and

$$R = T^t S^t S T \tag{12}$$

$$\gamma = \frac{T^t S^t S x}{\|Sx\|} \tag{13}$$

where (R, γ) are computed using the full set of possible views to be considered.

Fig. 1(b) illustrates how $(R_\Omega, \gamma_\Omega)$ are computed by selecting the rows and columns of (R, γ) corresponding to the chosen subset, Ω, of the complete set of $K_{\max}$ views. The value of VCL is then computed from $(R_\Omega, \gamma_\Omega)$. Notice that the computation of VCL requires a matrix inversion so it is $\mathcal{O}(K^3)$, but since $K < K_{\max}$, this computation is not expensive.

C. VCL Interpretation

In order to better understand the VCL, consider a measurement model with the form

$$y = T^t(\tilde{x} + \epsilon)$$

where y is the vector of observations, T is the matrix of bases, $\tilde{x}$ is the unknown object, and $\epsilon \sim \mathcal{N}(0, I)$ is white Gaussian noise with unit variance. Furthermore, define a linear function $\tilde{x} = c\,\eta$ where $\eta \in \mathbb{R}$ and $c \in \mathbb{R}^N$.

Then in the Supplementary Material, we show that the Fisher information for the estimation of $\tilde{x}$ given y is given by

$$\mathcal{I}_{\tilde{x}} = T R^{-1} T^t$$

and the Fisher information for the estimation of η is given y is given by

$$\mathcal{I}_\eta = c^t T R^{-1} T^t c.$$

Then if we choose $c = x/\|x\|$ where x is the reference object, we get the following expression for the Fisher information

$$\mathcal{I}_{VCL} = \gamma^t R^{-1} \gamma = 1 - VCL.$$

So, from this we can see that minimizing the VCL has the interpretation of maximizing the Fisher information for the estimation of the scalar quantity η when $\tilde{x} = x\eta$ where x is the reference object and $\tilde{x}$ is the unknown reconstruction.

This Fisher information can also be interpreted as maximizing the quadratic form given by

$$\mathcal{I}_{VCL} = \gamma^t B \gamma \tag{14}$$

where $B = R^{-1}$ is a precision matrix.

So this raises the question of how to interpret maximization of the view information, $\mathcal{I}_{VCL}$? First, maximizing the components of γ_Ω will increase the view information. This is intuitive, since a view that is correlated with x should collect more information about x.

The matrix $B = R^{-1}$ can be interpreted as a precision matrix that encodes the inverse covariance of the view-basis functions. Without loss of generality, we can again assume that the reconstruction bases are normalized so that, $\|T_{\theta_k}\| = 1$, in which case $\text{diag}\{R_\Omega\} = I$. Then the off-diagonal elements of B reflect the degree to which different views can be predicted from each other. Large negative off-diagonal values indicate strong mutual predictability; so B acts to penalize redundancy among views.

Consequently, maximizing $\mathcal{I}_{VCL}$ favors the selection of views that are both informative and diverse, which is precisely what view selection should do. Importantly, VCL incorporates both information and diversity in a natural way without requiring separate *ad hoc* weighted functions for these two purposes.

Algorithm 1: View Covariance Loss Selection Algorithm.

Function: VCLS$(\Omega, x; K, r_1, r_2)$
Output: Ω^*
// Step 1: Compute the reconstruction bases
$S \leftarrow$ RandSubsampleMatrix(x, r_1)
for i in 1 to $|\Omega|$ do:
  $T_{\theta_i} \leftarrow A_{\theta_i}^t H A_{\theta_i} x$
  $T_{\theta_i} \leftarrow S T_{\theta_i} / \|S T_{\theta_i}\|$
$x \leftarrow Sx$
// Step 2: Compute (R, γ)
for i in 1 to $|\Omega|$ do:
  $\gamma[i] \leftarrow T_{\theta_i}^t x / \|x\|$
  for j in 1 to $|\Omega|$ do:
    $R[i][j] \leftarrow T_{\theta_i}^t T_{\theta_j}$
// Step 3: Optimized View Selection
$\Omega^* \leftarrow$ ViewSubsetSelection$(\Omega, R, \gamma; K, r_2)$
return Ω^*

IV. View Covariance Loss Selection (VCLS)

In this section, we describe an implementation for the View Covariance Loss Selection (VCLS) algorithm which approximately minimizes the VCL in order to select the best view subset. The general strategy of the VCLS algorithm is to first compute (R, γ) for the full set of $K_{\max}$ possible views. The algorithm then searches through possible view subsets of size K to find the subset Ω^* that approximately minimizes $L(R_{\Omega^*}, \gamma_{\Omega^*})$. Since this requires a search through $\binom{K_{\max}}{K}$ possible subsets, we use a randomized search strategy to find an approximate minimum to the loss.

Authorized licensed use limited to: Purdue University. Downloaded on September 14,2026 at 09:10:02 UTC from IEEE Xplore. Restrictions apply.

Algorithm 2: View Subset Selection.

Function: ViewSubsetSelection$(\Omega, R, \gamma; K, r_2)$
Output: Ω^*
// Initialize with uniformly sampled view angles
$\Omega^* \leftarrow \text{UniformSampling}(K, \Omega)$
// Compute the initial loss value using Algorithm 3
$L^* \leftarrow \text{VCL}(R, \gamma, \Omega^*)$
// Test random view swaps
Repeat until no change:
  for $\theta_i \in \Omega^*$ do:
    $\Omega_S \leftarrow \text{RandomSampling}(r_2, \Omega - \Omega^*)$
    for $\theta_j \in \Omega_S$ do:
      $\Omega' \leftarrow \text{SwapAngle}(\Omega^*, \theta_i, \theta_j)$
      $L' \leftarrow \text{VCL}(R, \gamma, \Omega')$
      if $L' < L^*$ do
        $\Omega^* \leftarrow \Omega'$
        $L^* \leftarrow L'$
return Ω^*

Algorithm 3: Compute View Covariance Loss.

Function: $\text{VCL}(R, \gamma, \Omega)$
Output: L
// Subsample
$R_\Omega \leftarrow \text{Subsampling}(R, \Omega)$
$\gamma_\Omega \leftarrow \text{Subsampling}(\gamma, \Omega)$
// Compute Loss
$L \leftarrow 1 - \gamma_\Omega^t R_\Omega^{-1} \gamma_\Omega$
return L

Algorithm 1 first computes a random subsampling matrix as described in Section III-B above. Here, $0 < r_1 \leq 1.0$ is the spatial subsampling rate, which controls the trade-off between computational complexity and accuracy. The sampled voxels are selected within the region of interest (ROI), and for our experiments, the ROI is defined as the smallest sphere enclosing the reference object. However, the ROI can be user-defined based on specific application requirements. In practice, S can simply be represented by a list of indices corresponding to the sampled voxels.

Next, the subsampled reference image and reconstruction bases are computed.[1] While subsampling can be applied after the reconstruction bases are computed, some reconstruction packages allow for faster back projection of sparse voxel subsets [19]. In either case, the computation of these bases can be parallelized across independent processors. Step 2 of Algorithm 1 then computes (R, γ) from the subsampled bases, and Step 3 calls the ViewSubsetSelection() function to determine the best set of views.

Algorithm 2 is used to compute an optimized subset of K views, Ω^*, from the full set of views, Ω. This is done by first selecting a random subset of views, Ω^*. Then for each view in Ω^*, we attempt to identify a substitute view that results in a lower VCL. Specifically, for each view in Ω^*, a random subset Ω_S of size $\lfloor r_2(K_{\max} - K) \rfloor$ is generated from $\Omega \setminus \Omega^*$, where r_2 is the parameter that controls the trade-off of computation and thoroughness for each iteration. In each swap, a single view from Ω^* is exchanged with one from Ω_S. If the swap lowers the VCL, then Ω^* and its corresponding loss are updated accordingly, and this is continued until no change occurs after attempting random swaps for every angle in Ω^*.

Algorithm 3 evaluates the VCL. Notice that this algorithm first selects the relevant rows and columns of R and the elements of γ to form $(R_\Omega, \gamma_\Omega)$. This reduces computation since the (R, γ) only need to be computed once.

[1] Additional details on the generation of the reconstruction bases for the cone-beam reconstruction problem are provided in the Supplementary Material.

TABLE I
PARAMETERS FOR SIMULATED CT EXPERIMENT

Specification	Value
Geometry	cone-beam
Detector Dimensions (pixels)	1000×1000
Pixel Pitch in Detector (mm)	0.127
Source-to-Detector Distance (mm)	808.793
Source-to-Center of Rotation Distance (mm)	110.044
Maximum Energy of X-ray Source (keV)	200
Ground Truth Material	Iron
MBIRJAX Params - (sharpness, snr_db)	$(1.0, 35.0)$
Recon Array Size (slice first)	$1000 \times 1000 \times 1000$
Voxel Pitch in Object (mm)	0.017
VCLS Params (default)	$r_1 = 0.001$, $r_2 = 0.1$

V. EXPERIMENTAL RESULTS

In this section, we compare the effectiveness of the VCLS algorithm for view selection to both conventional uniform view sampling methods and the edge projection-based view selection (EPVS) algorithm of [20] for both simulated and measured X-ray CT datasets.

A. Simulated Data

In this section, we compare VCLS to EPVS and uniform view sampling using a simulated dataset. This allows us to compare to the exact ground truth.

Table I specifies the parameters used for generating and reconstructing the simulated cone-beam CT data. Additional details on the modeling of polychromatic X-ray effects, beam-hardening correction [39], and material modeling [40] are provided in the Supplementary Material.

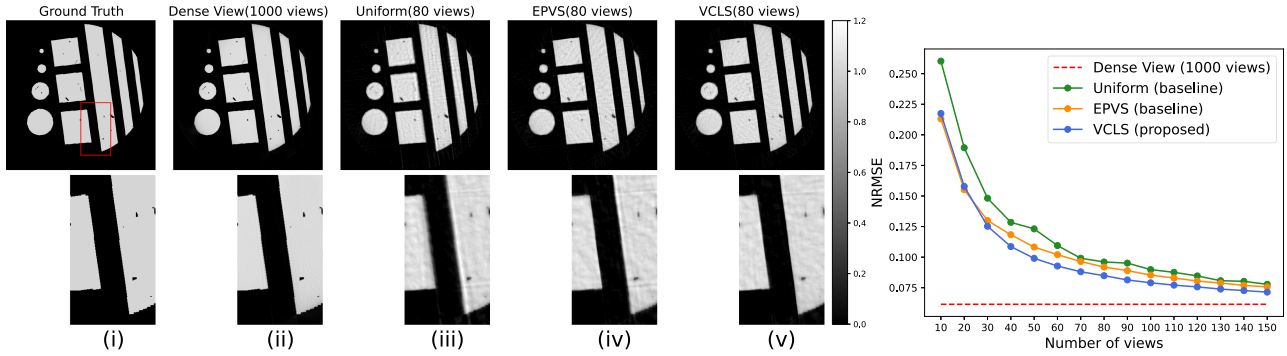
Fig. 2(a) shows the CAD model that was used to generate the ground truth and reference objects used in our simulations. The ground truth object was generated by rastering a CAD model using the parameters in Table I. This CAD model included extra artificial defects, such as pores and cracks embedded within the object. The reference object is similar, but not exactly the same, as the ground-truth object. This was done to test the robustness of our method. More specifically, we generated the reference object by rasterizing a second CAD without defects but with a slightly different rotation. We then rotated the reference object in 2D to visually match the position of the ground-truth object.

Fig. 2(b) and (c) show axial slices of both the ground truth and reference objects. A total of 720 candidate view angles

Authorized licensed use limited to: Purdue University. Downloaded on September 14,2026 at 09:10:02 UTC from IEEE Xplore. Restrictions apply.

TABLE II
VCLS COMPARISON FOR DIFFERENT (r_1, r_2) WITH $K = 100$ AND $K_{\max} = 720$

	$r_1 = 1.0, r_2 = 1.0$	$r_1 = 0.01, r_2 = 0.5$	$r_1 = 0.001, r_2 = 0.1$	$r_1 = 0.0001, r_2 = 0.01$
Step1: compute reconstruction bases	11.60 minutes	8.13 minutes	5.07 minutes	4.64 minutes
Step2: Compute (R, γ)	456.01 minutes	7.24 minutes	1.51 minutes	0.26 minutes
Step3: Compute View Subset Selection	2.93 minutes	2.21 minutes	0.39 minutes	0.04 minutes
Total Time	470.54 minutes	17.58 minutes	6.97 minutes	4.94 minutes
Reconstruction Error (NRMSE)	0.0780	0.0792	0.0794	0.0801



(a) Reconstruction (b) Reconstruction loss

Fig. 3. Comparison of view selection methods using simulated cone-beam axial CT data. (a) Axial MBIR reconstructions with the top row being the full slice and the bottom row being zoomed-in portion in red rectangle. (i) Ground truth; (ii) 1000 uniformly sampled views; (iii) 80 uniformly sampled views; (iv) 80 EPVS sampled views; and (v) 80 VCLS sampled views. (b) Plot of NRMSE for VCLS, EPVS, and uniform view sampling. Notice that VCLS produces consistently low NRMSE with sharper edges and more refined texture detail than either uniform sampling or EPVS.

were uniformly sampled from the range of 0° to 360° for view selection.

Unless otherwise noted, all reconstructions used MBIR via the MBIRJAX software package [19], and all experiments were performed on 2 A100 GPUs and a 64-core CPU platform using a combination of python, numpy, and JAX software environments. MBIRJAX automatically controls regularization using the meta-parameters of snr_db and sharpness specified in Table I.

Table II compares the runtime and reconstruction loss of VCLS using different values of r_1 and r_2.[2] Notice that as r_1 and r_2 decrease, the computation time decreases, but the reconstruction error increases slightly. We found $(r_1, r_2) = (0.001, 0.1)$ to be a good trade-off, and used these values in all remaining experiments.

Fig. 3(a) shows comparisons of VCLS with uniform view sampling and the EPVS algorithm [20] for the simulated cone-beam data. The axial slices shown in Fig. 3(a) demonstrate that VCLS results in sharper edges and more refined texture detail than either uniform sampling or EPVS. The plot of NRMSE versus number of views in Fig. 3(b) supports this by showing that the VCLS reconstructions have lower NRMSE than the uniform or EPVS reconstructions as the number of views varies from 30 to 150.

B. Measured Data

We next compare VCLS with EPVS and uniform view sampling using an experimentally measured axial cone-beam X-ray CT data scan of a hexagonal fuel nozzle [41] collected on a ZEISS Metrotom 800 system. Table III lists the parameters used in the experiment. Fig. 6(b) shows an axial slice of the additively manufactured hexagonal object that was used in this experiment.

In AM inspection, it is typical for a sequence of parts printed from the same CAD drawing to be scanned consecutively. In such scenarios, the information gained from the first scanned part can be used to guide the scanning strategy for the remaining parts. To simulate this, a binary segmentation of the

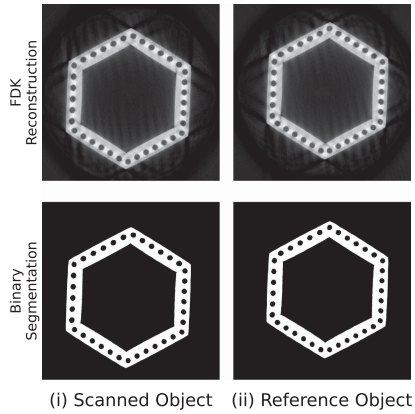


Fig. 4. Hexagonal fuel nozzle axial slice for (i) the object scanned in experiments; (ii) the reference object used for view selection. Top row: FDK reconstructions from dense view sampling. Bottom row: Segmentation of FDK reconstructions. The segmentation of the reference object was used as x in VCL evaluation. Notice that the scanned object and the reference object are not exactly the same with a slight positional shift and some differences in details.

[2]We note that Step 1 of Algorithm 1 used both GPUs and the sparse back-projection capability of MBIRJAX to speed computations.

Authorized licensed use limited to: Purdue University. Downloaded on September 14,2026 at 09:10:02 UTC from IEEE Xplore. Restrictions apply.

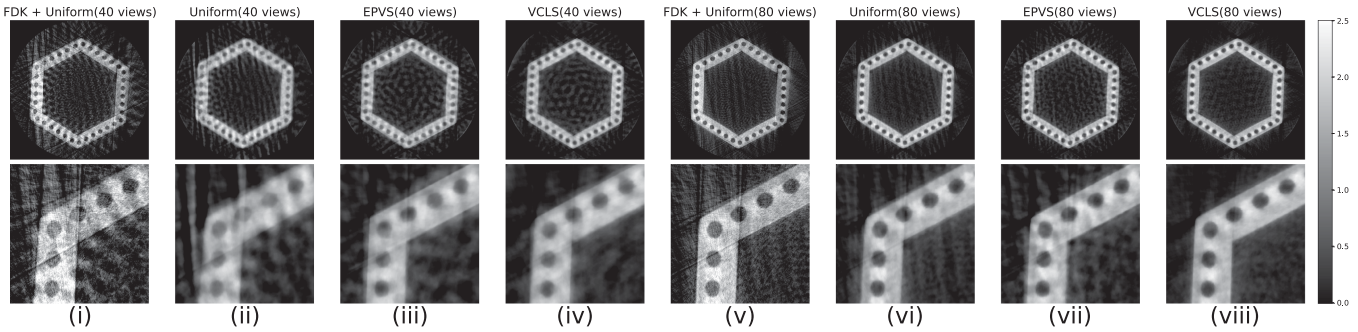


Fig. 5. Comparison of view selection methods using hexagonal fuel nozzle data. Top row is the full axial slice of reconstruction, and bottom row is a zoomed-in portion of the region outlined in red in Fig. 6(b). (i) 40 uniformly-sampled views + FDK (baseline method); (ii) 40 uniformly-sampled views + MBIR (baseline method); (iii) 40 EPVS sampled views + MBIR (baseline method); (iv) 40 VCLS sampled views + MBIR (proposed method). (v) 80 uniformly-sampled views + FDK (baseline method); (vi) 80 uniformly-sampled views + MBIR (baseline method); (vii) 80 EPVS sampled views + MBIR (baseline method); (viii) 80 VCLS sampled views + MBIR (proposed method). Notice that VCLS produces reconstructions with sharper edges and fewer artifacts.

TABLE III
PARAMETERS FOR FUEL NOZZLE CT EXPERIMENT

Specification	Value
Instrument	ZEISS Metrotom 800
Geometry	cone-beam
Detector Dimensions (pixels)	1024×1024
Pixel Pitch in Detector (mm)	0.2
Source-to-Detector Distance (mm)	808.508
Source-to-Center of Rotation Distance (mm)	243.307
Maximum Energy of X-ray Source (keV)	180
Scanned Object Material	316L stainless steel
MBIRJAX Params - (sharpness, snr_db)	$(1.0, 35.0)$
Recon Array Size (slice first)	$893 \times 1008 \times 1008$
Voxel Pitch in Object (mm)	0.06
VCLS Params (default)	$r_1 = 0.001, r_2 = 0.1$

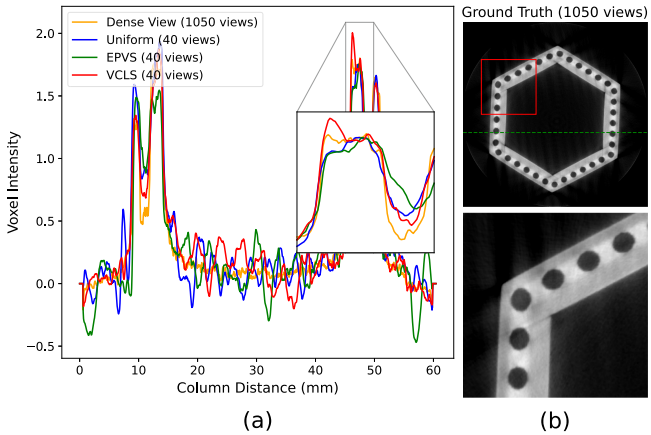


Fig. 6. Hexagonal fuel nozzle (a) intensity profiles; (b) ground truth from MBIR reconstruction using 1050 uniformly sampled views. Red box indicates zoomed-in region and green line indicates line used for intensity profile.

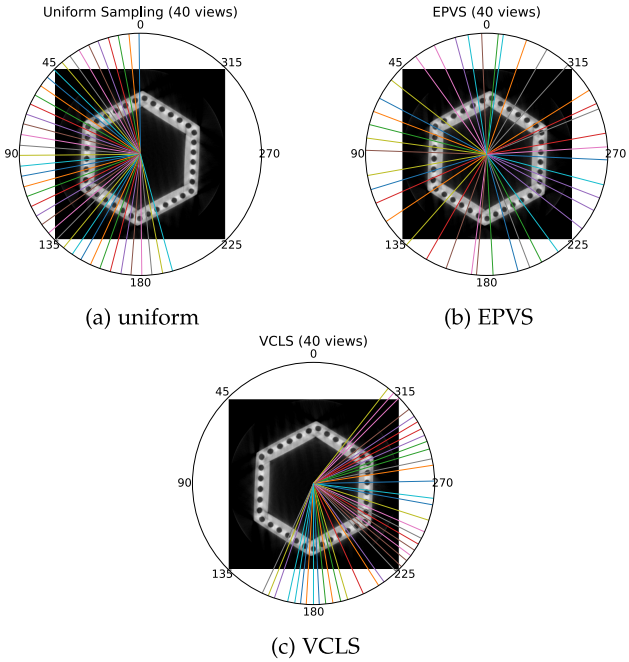


Fig. 7. Illustration of the 40 selected views using radial lines for hexagonal fuel nozzle data using (a) uniform sampling (short scan), (b) EPVS, and (c) VCLS. Notice both EPVS and VCLS select views with non-uniform spacing. However, VCLS automatically selects views with a narrower angular range (less than 180°).

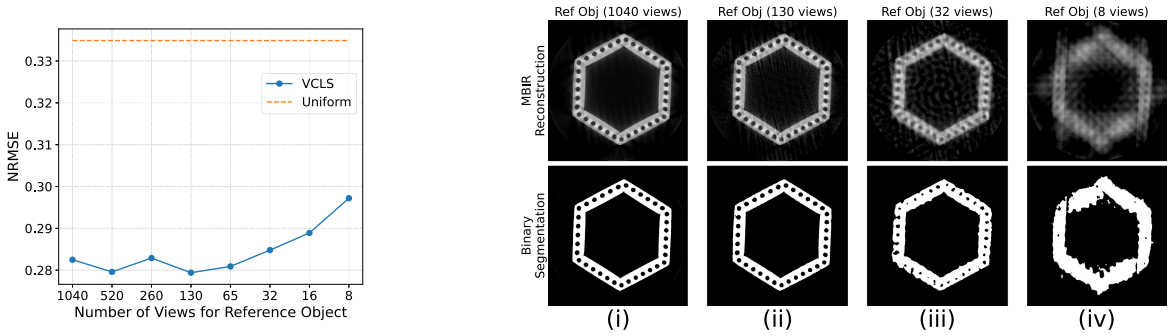
reconstructed image from a dense-view scan of a separate object is used as the reference object for view selection.

Fig. 4 shows the scanned object and the reference object. Notice that the reference object does not perfectly match the scanned object, which tests the robustness of view selection under imperfect reference object conditions.

From Tuy's condition [2], [3], it is known that views from $0°$ to $180°$ plus the cone angle (short scan) are sufficient for complete Fourier space coverage. Therefore, in order to achieve the best results, our uniform sampling uses equally spaced samples in the range of $[0°, 194.42°]$, where the cone angle is $14.42°$ in our setting. However, the VCLS and EPVS algorithms are allowed to select views from the full range of $[0°, 360°]$ for maximum flexibility.

Unless otherwise noted, all reconstructions were performed using MBIRJAX on an A100 GPUs and a 64-core CPU platform with the parameters listed in Table III. Any FDK reconstructions of short scan data used Parker weighting to improve reconstruction quality and avoid corresponding short scan artifacts [42].

Authorized licensed use limited to: Purdue University. Downloaded on September 14,2026 at 09:10:02 UTC from IEEE Xplore. Restrictions apply.



(a) Reconstruction loss (b) Reference objects

Fig. 8. (a) Plot of reconstruction loss (NRMSE) for 40-view reconstructions using VCLS sampling, but with varying reference object quality. The dashed line shows baseline NRMSE with 40 uniformly sampled views. (b) Examples of reference objects generated by reconstructing the actual object from uniformly sampled sparse views ranging from 1040 views to 8 views. The top row shows the full axial slice of each reconstruction, and the bottom row shows the corresponding segmentation. Note that VCLS consistently outperforms uniform sampling even when the quality of the reference object is quite poor.

TABLE IV
FWHM WIDTHS FROM FUEL NOZZLE DATA

	Uniform		EPVS		VCLS	
num. views	width (mm)	error (mm)	width (mm)	error (mm)	width (mm)	error (mm)
1050	2.34	0	\	\	\	\
40	2.70	0.36	3.18	0.84	2.46	**0.12**
80	2.46	0.12	1.92	-0.42	2.34	**0.00**

TABLE V
HOLE DIAMETERS FROM FUEL NOZZLE DATA

	Uniform		EPVS		VCLS	
num. views	dia. (mm)	error (mm)	dia. (mm)	error (mm)	dia. (mm)	error (mm)
1050	1.89 $\pm$ 0.05	0	\	\	\	\
40	1.08 $\pm$ 0.47	0.81	1.34 $\pm$ 0.30	0.55	1.59 $\pm$ 0.11	**0.30**
80	1.76 $\pm$ 0.08	0.13	1.77 $\pm$ 0.06	0.12	1.79 $\pm$ 0.06	**0.10**

Fig. 5 shows the reconstructed images obtained using 40 and 80 selected views, which correspond to approximately a 26$\times$ and 13$\times$ reduction in the number of measurements compared to a dense scan of 1050 views. Notice that for both the 40 and 80 view case, the VCLS view selection produces sharper images with fewer artifacts than either uniform or EPVS view selection. Also, VCLS achieves much better quality than FDK reconstruction with uniform view sampling shown in Fig. 5(i) and (v).

To demonstrate the impact of such algorithm in real world application, we considered dimensional characterization of object width and holes using sparse view reconstruction algorithms. Such characterizations are critical in applications such as industrial metrology of parts that require accurate measurement of object dimensions.

Fig. 6 shows line profiles through the reconstructions along the green line shown in the dense-view reconstruction of Fig. 6(b). Then Table IV lists the associated measured values of the object's width using the full-width at half maximum (FWHM) measure. The associated error is also listed for each measurement using the measured width with dense view (1050 views) as ground truth.

Notice that in Table IV, VCLS has the lowest measured error in both the 40 view case (0.12 mm error) and in the 80 view case (0 mm error). This is consistent with the visual inspection of the line profiles for the 40 view case shown in Fig. 6. Here, the dense view result (yellow curve) is used as ground-truth.

Table V presents a summary of an analysis of the diameters of holes in the object. Notice that for both the 40 and 80 view case, the VCLS algorithm results in reconstructions with the lowest error in the mean diameter estimate. Moreover, the standard deviation of the error is the lowest among the alterative view selection algorithms. More details of the analysis are presented in the Supplementary Material.

Fig. 7 illustrates the view selection patterns for uniform sampling (using a short scan), EPVS, and VCLS. Note that VCLS selects views from a narrower range of angles used by EPVS or even the short scan predicted by Tuy's condition. This is potentially useful since it reduces the range of angles that must be obtained during a scan. Also, notice that the VCLS views are not uniformly spaced. Instead, there are subtle but important variations in view angle that appear to favor particularly informative views while also preserving view diversity.

C. *Effect of Reference Object Quality*

In this section, we investigate the effect of the reference object quality on the VCLS algorithm view selection using the measured data of Section V-B.

Fig. 8(a) plots the NRMSE using 40 views selected by VCLS, but based on a reference object of varying quality. Each reference object is generated by reconstructing the object from uniformly sampled sparse views, with sampling ranging from 1040 views to only 8 views. Fig. 8(b) shows the reference reconstructions used in the plot along with their corresponding segmentations.

Notice that the NRMSE of the VCLS reconstruction increases slowly, even for very low-quality reference reconstructions. In fact, the VCLS reconstruction is still much better than the baseline (uniform view sampling) reconstruction, even when the reference is reconstructed from only 8 uniformly sampled views. This suggests that it is possible to use even a fast ultra-sparse CT

Authorized licensed use limited to: Purdue University. Downloaded on September 14,2026 at 09:10:02 UTC from IEEE Xplore. Restrictions apply.

scan in order to generate a reference object of sufficient quality for use in the VCLS algorithm.

VI. Conclusion

We present an algorithm for CT view selection which is based on the minimization of a novel view covariance loss (VCL) function. The VCL is unique in that it is a single expression that accounts for the joint information in the views. We show that the VCL is closely related to the Fisher information for estimating a linear projection of the object, providing a principled justification for its use. Consequently, it encourages view selections that are both informative and diverse (i.e., uncorrelated). The VCL also has a relatively simple closed form and can be computed efficiently for practical CT problems using straightforward acceleration methods. Experimental results on both simulated and measured cone-beam CT data demonstrate that the view covariance loss selection (VCLS) algorithm selects views that differ subtly from uniform sampling, but that substantially improve the quality of CT reconstruction.

Acknowledgment

This work was co-authored by UT-Battelle, LLC under contract DE-AC05-00OR22725 with the US Department of Energy (DOE). The US government retains and the publisher, by accepting the article for publication, acknowledges that the US government retains a nonexclusive, paid-up, irrevocable, worldwide license to publish or reproduce the published form of this manuscript, or allow others to do so, for US government purposes. DOE will provide public access to these results of federally sponsored research in accordance with the DOE Public Access Plan (http://energy.gov/downloads/doe-public-access-plan).

References

[1] A. Thompson, I. Maskery, and R. K. Leach, "X-ray computed tomography for additive manufacturing: A review," *Meas. Sci. Technol.*, vol. 27, no. 7, 2016, Art. no. 072001.

[2] H. Tuy, "Reconstruction of a three-dimensional object from a limited range of views," *J. Math. Anal. Appl.*, vol. 80, no. 2, pp. 598–616, 1981.

[3] H. K. Tuy, "An inversion formula for cone-beam reconstruction," *SIAM J. Appl. Math.*, vol. 43, no. 3, pp. 546–552, 1983.

[4] G. N. Ramachandran and A. V. Lakshminarayanan, "Three-dimensional reconstruction from radiographs and electron micrographs: Application of convolutions instead of Fourier transforms," *Proc. Nat. Acad. Sci.*, vol. 68, no. 9, pp. 2236–2240, 1971.

[5] L. A. Feldkamp, L. C. Davis, and J. W. Kress, "Practical cone-beam algorithm," *JOSA A*, vol. 1, no. 6, pp. 612–619, 1984.

[6] H. Villarraga-Gómez and S. T. Smith, "Effect of the number of projections on dimensional measurements with X-ray computed tomography," *Precis. Eng.*, vol. 66, pp. 445–456, 2020.

[7] A. du Plessis and J. M. Waller, "Simple and standardised X-ray CT testing in metal additive manufacturing," *Metal Additive Manuf.*, vol. 30, 2021, Art. no. 100837. [Online]. Available: https://www.metal-am.com/articles/simple-and-standardised-x-ray-ct-testing-in-metal-3d-printing/

[8] J. Thibault, K. D. Sauer, C. A. Bouman, and J. Hsieh, "A three-dimensional statistical approach to improved image quality for multislice helical CT," *Med. Phys.*, vol. 34, no. 11, pp. 4526–4544, 2007.

[9] Z. Yu, C. A. Bouman, K. D. Sauer, and J. Hsieh, "Fast model-based X-ray CT reconstruction using spatially nonhomogeneous ICD optimization," *IEEE Trans. Image Process.*, vol. 20, no. 1, pp. 161–175, Jan. 2011.

[10] S. J. Kisner, E. Haneda, C. A. Bouman, S. Skatter, M. Kourinny, and S. Bedford, "Model-based ct reconstruction from sparse views," in *Proc. 2nd Int. Conf. Image Formation X-Ray Computed Tomogr.*, vol. 33, 2012, Art. no. 100558.

[11] T. Balke et al., "Separable models for cone-beam MBIR reconstruction," *Electron. Imag.*, vol. 2018, no. 15, pp. 181–1, 2018.

[12] S. V. Venkatakrishnan, C. A. Bouman, and B. Wohlberg, "Plug-and-play priors for model based reconstruction," in *Proc. IEEE Glob. Conf. Signal Inf. Process.*, 2013, pp. 945–948.

[13] S. Sreehari et al., "Plug-and-play priors for bright field electron tomography and sparse interpolation," *IEEE Trans. Comput. Imag.*, vol. 2, no. 4, pp. 408–423, Dec. 2016.

[14] G. T. Buzzard, S. Sreehari, V. Katkovnik, K. Egiazarian, C. A. Bouman, and B. Wohlberg, "Plug-and-play unplugged: Optimization-free reconstruction using consensus equilibrium," *SIAM J. Imag. Sci.*, vol. 11, no. 3, pp. 2001–2020, 2018.

[15] A. Ziabari et al., "Simurgh: A framework for CAD-driven deep learning based x-ray ct reconstruction," in *Proc. IEEE Int. Conf. Image Process.*, 2022, pp. 3836–3867.

[16] A. Ziabari et al., "Enabling rapid X-ray CT characterisation for additive manufacturing using CAD models and deep learning-based reconstruction," *Nature Comput. Mater.*, vol. 9, no. 1, 2023, Art. no. 91.

[17] "High aspect ratio tomography HART plus," *Bruker microCT*, Method Note MCT-123, 2019, Accessed: Apr. 07, 2025. [Online]. Available: https://www.foa.unesp.br/Home/pesquisa/escritoriodeapoioapesquisa/mn123_hartplus.pdf

[18] F. Bauer, M. Lang, T. Laue, B. Gottschall, S. Sievers, and S. Lanza, "Practical part-specific trajectory optimization for robot-guided inspection via computed tomography," *J. Nondestruct. Eval.*, vol. 41, no. 3, 2022, Art. no. 55.

[19] C. A. Bouman and G. T. Buzzard, "MBIRJAX: High-performance tomographic reconstruction," 2024, Accessed: Jun. 16, 2025. https://github.com/cabouman/mbirjax

[20] J. Lin, S. Venkatakrishnan, O. Rahman, G. T. Buzzard, A. Ziabari, and C. A. Bouman, "An adaptive view selection algorithm for large-scale cone-beam CT reconstruction," in *Proc. 14th Conf. Ind. Computed Tomogr.*, Antwerp, Belgium, 2025, pp. 1–9.

[21] C. A. Bouman and G. T. Buzzard, "MBIRJAX applications," 2024, accessed: Jun. 16 2025. https://github.com/cabouman/mbirjax_applications

[22] K. J. Batenburg, W. J. Palenstijn, P. Balázs, and J. Sijbers, "Dynamic angle selection in binary tomography," *Comput. Vis. Image Understanding*, vol. 117, no. 4, pp. 306–318, 2013.

[23] M. A. Haque, M. O. Ahmad, M. N. S. Swamy, M. K. Hasan, and S. Y. Lee, "Adaptive projection selection for computed tomography," *IEEE Trans. Image Process.*, vol. 22, no. 12, pp. 5085–5095, Dec. 2013.

[24] A. Presenti, J. Sijbers, and J. De Beenhouwer, "Dynamic few-view x-ray imaging for inspection of CAD-based objects," *Expert Syst. Appl.*, vol. 180, 2021, Art. no. 115012.

[25] A. Matz, W. Holub, and R. Schielein, "Trajectory optimization in computed tomography based on object geometry," in *Proc. 11th Conf. Ind. Comput. Tomogr.*, Wels, Austria, 2022, pp. 1–5.

[26] D. Yang et al., "An edge alignment-based orientation selection method for neutron tomography," in *Proc. IEEE Int. Conf. Acoust., Speech Signal Process.*, 2023, pp. 1–5.

[27] J. Lin, S. Venkatakrishnan, G. Buzzard, A. K. Ziabari, and C. Bouman, "Edge projection-based adaptive view selection for cone-beam ct," 2024, *arXiv:2407.12963*.

[28] C. Heinzl, S. Reh, J. Kastner, D. Salaberger, and J. Georgi, "Optimal specimen placement in cone beam X-ray computed tomography," *NDT E Int.*, vol. 50, pp. 42–49, 2012.

[29] T. Kano and M. Koseki, "Optimization of multi-axis control for metal artifact reduction in X-ray computed tomography," in *Proc. 9th Conf. Ind. Comput. Tomogr.*, Padova, Italy, 2019, pp. 1–6.

[30] T. Ito, Y. Ohtake, and H. Suzuki, "Orientation optimization and jig construction for X-ray CT scanning," *NDT:net*, vol. 10, 2020, Art. no. 220.

[31] N. Brierley, C. Bellon, and B. L. Toralles, "Optimized multi-shot imaging inspection design," in *Proc. Roy. Soc. A: Math., Phys. Eng. Sci.*, vol. 474, no. 2216, 2018, Art. no. 20170319.

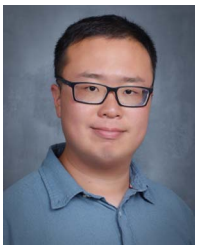
[32] N. Brierley, "Optimised inspection of complex geometries," in *Proc. 12th Eur. Conf. Non-Destructive Testing*, Gothenburg, Sweden, 2018, pp. 1–5.

[33] D. Suth, N. Grozmani, R. H. Schmitt, F. Helmli, and J. Kastner, "Automatic scan planning for CT scans," in *Proc. 11th Conf. Ind. Computed Tomogr.*, Wels, Austria, 2022, pp. 1–7.

[34] A. Fischer et al., "Object specific trajectory optimization for industrial X-ray computed tomography," *Sci. Rep.*, vol. 6, 2016, Art. no. 19135.

Authorized licensed use limited to: Purdue University. Downloaded on September 14,2026 at 09:10:02 UTC from IEEE Xplore. Restrictions apply.

[35] Z. Shen, Y. Wang, D. Wu, X. Yang, and B. Dong, "Learning to scan: A deep reinforcement learning approach for personalized scanning in CT imaging," 2020, *arXiv: 2006.02420*.
[36] T. Wang, F. Lucka, and T. van Leeuwen, "Sequential experimental design for X-ray CT using deep reinforcement learning," 2023, *arXiv:2307.06343*.
[37] P. Yang and B. Dong, "L2SR: Learning to sample and reconstruct for accelerated MRI via reinforcement learning," *Inverse Problems*, vol. 40, 2024, Art. no. 055015.
[38] J. Hsieh, *Computed Tomography: Principles, Design, Artifacts, and Recent Advances*, 4th ed.Bellingham, WA, USA: SPIE, 2021.
[39] Y. Kyriakou, E. Meyer, D. Prell, and W. A. Kalender, "Empirical beam hardening correction (EBHC) for CT," *Med. Phys.*, vol. 37, no. 10, pp. 5179–5187, 2010.
[40] J. H. Hubbell and S. M. Seltzer, "Tables of X-ray mass attenuation coefficients and mass energy-absorption coefficients 1 kev to 20 mev for elements z = 1 to 92 and 48 additional substances of dosimetric interest," National Institute of Standards and Technology (NIST) *Standard Reference Database 126*, 1995, Accessed: Apr. 04, 2025. [Online]. Available: https://www.nist.gov/pml/x-ray-mass-attenuation-coefficients
[41] A. Ziabari, O. Rahman, S. Venkatakrishnan, and R. Dehoff, "X-ray computed tomography data of dense metallic components," 2025. [Online]. Available: https://doi.org/10.13139/ORNLNCCS/2568789
[42] D. L. Parker, "Optimal short scan convolution reconstruction for fanbeam CT," *Med. Phys.*, vol. 9, no. 2, pp. 254–257, Mar. 1982.



Jingsong Lin (Graduate Student Member, IEEE) received the BS degree in electrical engineering from the Beijing Institute of Technology, Beijing, China, and the Australian National University, Canberra, Australia, in 2018, and the MS degree in electrical engineering from Cornell University, Ithaca, NY, USA, in 2019. He is currently working toward the PhD degree in electrical engineering with Purdue University, West Lafayette, IN, USA. His research interests include computational imaging, inverse problems, and signal processing.



Amirkoushyar Ziabari (Senior Member, IEEE) received the PhD degree from the department of ECE at Purdue University, in 2016. He is a senior R&D staff scientist in the Multimodal Sensor Analytics group with the Electrification and Energy Infrastructure Division (EEID), with the Oak Ridge National Laboratory (ORNL). Before joining ORNL, he was a Postdoc in the Integrated Imaging group with the Department of Electrical and Computer Engineering (ECE), Purdue University. His research interests have been at the intersection of physics, signal processing and machine/deep learning, where he has used image/signal processing and machine learning (ML) ideas to explore multiscale experimental physics phenomena. He is currently working on data analytic, data driven and physics-based image reconstruction and segmentation for advanced manufacturing (AM) in order to improve non-destructive evaluation (NDE) and the state-of-the-art in real time monitoring of the AM process. Dr. Ziabari is also leading several other projects on developing ML and computational imaging algorithms for image analysis and reconstruction in scientific imaging, including electron microscopy, electron tomography, neutron CT, coded-aperture imaging, etc. Dr. Ziabari is a member of the IEEE Computational Imaging Technical Committee.



Singanallur V. Venkatakrishnan (Senior Member, IEEE) received the PhD degree from the School of Electrical and Computer Engineering, Purdue University, West Lafayette, IN, USA, in 2014. He is currently a senior R&D staff member with Multimodal Sensor Analytics Group, Oak Ridge National Laboratory developing computational imaging algorithms in support of the lab's efforts in ultrasound, X-ray, electron and neutron-based systems. His research interests include computational imaging, inverse problems, and machine learning. Dr. Venkatakrishnan is a Senior Area Editor of IEEE Transaction On Computational Imaging.



Obaidullah Rahman received the BTech degree in electronics engineering from Aligarh Muslim University, the MS and PhD degrees in electrical engineering from the University of Notre Dame. He is a Data Analytics Researcher with Oak Ridge National Laboratory, specializing in computational imaging, X-ray computed tomography (CT), and electron microscopy. His research spans deep learning algorithms for CT reconstruction, defect characterization in additive manufacturing, and characterization of fuel cell microscopy samples. Obaidullah has done internship at General Electric Healthcare where he worked on low-dose medical CT images and developed analytical and deep learning solutions to combat low-SNR artifacts.



Gregery T. Buzzard (Senior Member, IEEE) received the PhD degree from the University of Michigan, Ann Arbor, MI, USA. He was a postdoctoral with Indiana University, Bloomington, IN, USA, and Cornell University, Ithaca, NY, USA. He is currently a professor of mathematics and the director of the Center for Computational and Applied Mathematics with Purdue University, West Lafayette, IN, USA, where he was the Mathematics Department Head for seven years. His research has led to theoretical advances in dynamical systems and experiment design and to new algorithms for image and volume reconstruction for a variety of sensing modalities. The unifying ideas in his recent work are iterative methods for image reconstruction and reduction of uncertainty through appropriate measurement schemes.



Charles A. Bouman (Life Fellow, IEEE) received the BSEE degree from the University of Pennsylvania, MS degree from the University of California at Berkeley, and the PhD degree from Princeton University, in 1989. He is the Showalter professor of Electrical and Computer Engineering and Biomedical Engineering at Purdue University. His research in computational imaging is focused on the integration of statistical signal processing, physics, and computation to solve problems with applications in healthcare, scientific, industrial, and consumer imaging. He is a member of the National Academy of Inventors, a Fellow and Honorary Member of the IS&T, and a Fellow of SPIE and AIMBE. He is currently a vice president of the IS&T. From 2000 to 2004, he served as the vice President of Publications for the IS&T. In 2022, he was made an Honorary Member of the IS&T, and in 2023, he was given the IS&T Service Award. He received the 2021 IEEE Signal Processing Society, Claude Shannon-Harry Nyquist Technical Achievement Award, the 2014 Electronic Imaging Scientist of the Year award, and in 2020, his paper on Plug-and-Play Priors won the SIAM Imaging Science Best Paper Prize. In 2003, he founded the IS&T Computational Imaging Conference and led the creation of the IEEE Transactions on Computational Imaging.

Authorized licensed use limited to: Purdue University. Downloaded on September 14,2026 at 09:10:02 UTC from IEEE Xplore. Restrictions apply.